ACS Infectious Diseases

pubs.acs.org/journal/aidcbc

Article

Enzymatic β-Oxidation of the Cholesterol Side Chain in *Mycobacterium tuberculosis* Bifurcates Stereospecifically at Hydration of 3-Oxo-cholest-4,22-dien-24-oyl-CoA

Tianao Yuan,[‖] Joshua M. Werman,[‖] Xingyu Yin,[‖] Meng Yang, Miguel Garcia-Diaz, and Nicole S. Sampson*

Cite This: *ACS Infect. Dis.* 2021, 7, 1739−1751

Read Online

ACCESS | Metrics & More | Article Recommendations | Supporting Information

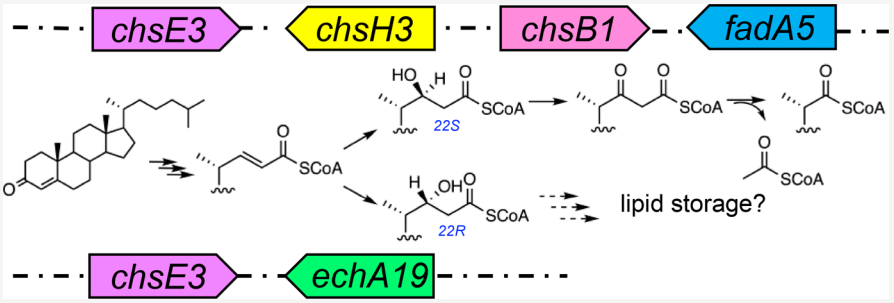

ABSTRACT: The unique ability of *Mycobacterium tuberculosis* (Mtb) to utilize host lipids such as cholesterol for survival, persistence, and virulence has made the metabolic pathway of cholesterol an area of great interest for therapeutics development. Herein, we identify and characterize two genes from the Cho-region (genomic locus responsible for cholesterol catabolism) of the Mtb genome, *chsH3* (Rv3538) and *chsB1* (Rv3502c). Their protein products catalyze two sequential stereospecific hydration and dehydrogenation steps in the β-oxidation of the cholesterol side chain. ChsH3 favors the 22*S* hydration of 3-oxo-cholest-4,22-dien-24-oyl-CoA in contrast to the previously reported EchA19 (Rv3516), which catalyzes formation of the (22*R*)-hydroxy-3-oxo-cholest-4-en-24-oyl-CoA from the same enoyl-CoA substrate. ChsB1 is stereospecific and catalyzes dehydrogenation of the ChsH3 product but not the EchA19 product. The X-ray crystallographic structure of the ChsB1 apo-protein was determined at a resolution of 2.03 Å, and the holo-enzyme with bound NAD^+ cofactor was determined at a resolution of 2.21 Å. The homodimeric structure is representative of a classical NAD^+-utilizing short-chain type alcohol dehydrogenase/reductase, including a Rossmann-fold motif, but exhibits a unique substrate binding site architecture that is of greater length and width than its homologous counterparts, likely to accommodate the bulky steroid substrate. Intriguingly, Mtb utilizes hydratases from the MaoC-like family in sterol side-chain catabolism in contrast to fatty acid β-oxidation in other species that utilize the evolutionarily distinct crotonase family of hydratases.

KEYWORDS: *Mycobacterium tuberculosis, cholesterol, catabolism, stereochemistry, Rv3538, Rv3502c*

Mycobacterium tuberculosis (Mtb) infects one-fourth of the world population and is the etiologic agent that causes tuberculosis (TB). When the host is coinfected with HIV, TB causes severe morbidity.[1] Progress over the last 5 years for reduced TB incidence and deaths as part of the World Health Organization's End TB Strategy for 2030 in conjunction with the United Nations Sustainable Development Goals (SDGs) has been moderate.[1] Furthermore, the effects of the COVID-19 pandemic are expected to erase this modest progress with an anticipated increase of 1 million deaths per year from TB over the next five years.[1] As part of multifactorial solutions to the TB pandemic, shorter and simpler treatments for TB disease are required.[2]

Mtb utilizes an array of carbon sources in the host for survival and persistence,[3,4] including cholesterol, whose metabolism plays an essential role in Mtb's virulence and pathogenesis.[5] During the last 15 years, many cholesterol-metabolism-associated genes that are crucial for the survival and virulence of Mtb have been identified and characterized.[6] Different strategies have been developed to selectively target cholesterol metabolism in Mtb,[7,8] and these cholesterol-metabolism-associated genes and their protein products have proven vulnerable to small-molecule inhibition for potential TB therapeutic intervention.[9,10]

Received: February 7, 2021
Published: April 7, 2021

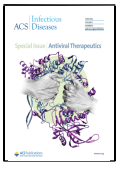

Scheme 1. Proposed Reactions in the Second β-Oxidation Cycle of the Mtb Cholesterol Side-Chain Catabolism

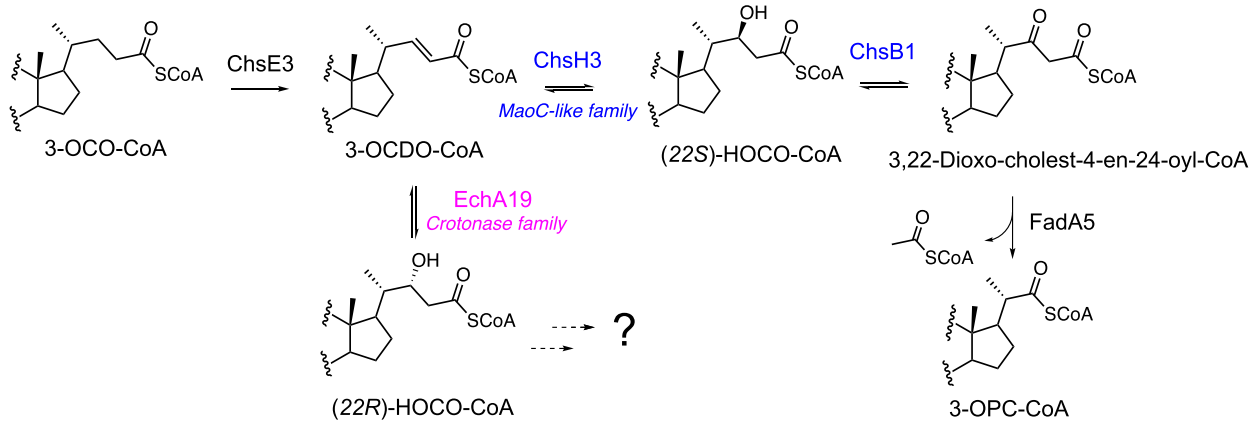

Mtb does not synthesize cholesterol but maintains the ability to import and utilize host-derived cholesterol during infection from, for example, colocalized macrophages.[4,5] Mtb engages at least three distinct subpathways for cholesterol catabolism, i.e., side-chain degradation, A&B ring degradation, and C&D ring degradation.[11] The metabolites of cholesterol degradation, i.e., acetyl-CoA, propionyl-CoA, succinyl-CoA, and pyruvate, are further incorporated into metabolic pathways for energy production and lipid biosynthesis in Mtb.[12−14]

In Mtb and other steroid-utilizing actinomycetes, the alkyl side chain of cholesterol is largely degraded through a series of β-oxidation reactions. These processes are analogous to fatty acid degradation in mammals and bacteria. In a typical fatty acid β-oxidation cycle, a fatty acyl-CoA thioester first undergoes β-dehydrogenation catalyzed by an acyl-CoA dehydrogenase. Then, an enoyl-CoA hydratase catalyzes the hydration of the 2-enoyl-CoA resulting in a 3-hydroxyacyl-CoA ester. Next, oxidation of the hydroxylacyl-CoA is catalyzed by a hydroxyacyl-CoA dehydrogenase to produce a 3-ketoacyl-CoA ester. Last, the 3-ketoacyl-CoA undergoes retro-Claisen cleavage catalyzed by a β-ketothiolase to release an acetyl-CoA and regenerate a two-carbon shortened acyl-CoA thioester.

The genes that encode enzymes involved in the cholesterol side-chain catabolism in the Mtb genome are transcriptionally regulated by the repressor KstR1.[15,11] In this work, we sought to identify and characterize cholesterol side-chain degrading enzymes from the KstR1 regulon in Mtb. Among the essential genes required for Mtb's growth on cholesterol in vitro, we investigated the catalytic activity of the gene products of Rv3538 and Rv3502c, which we will refer to as *chsH3* and *chsB1* respectively to emphasize their newly established functions in Mtb cholesterol side-chain degradation. We employed biophysical, biochemical, and steady-state kinetic characterizations to determine the role of ChsH3 and ChsB1 in cholesterol side-chain degradation. Furthermore, we characterized the structure of ChsB1 through crystallography to further understand the steroid hydroxyl dehydrogenation process in Mtb.

Our data clearly demonstrate that ChsH3 is a MaoC-like family hydratase[16] catalyzing stereospecific hydration of 3-oxo-chol-4,22-dien-24-oyl-CoA (3-OCDO-CoA), the enoyl-CoA formed in the second cycle of cholesterol side-chain β-oxidation (Scheme 1). ChsH3 catalyzes formation of the 22*S* diastereomer of 22-hydroxy-3-oxo-cholest-4-en-24-oyl-CoA (22-HOCO-CoA), whereas the previously reported EchA19, also in the KstR1 regulon, catalyzes formation of the 22*R* diastereomer. Furthermore, ChsB1 is the 3-hydroxy acyl-CoA dehydrogenase responsible for catalyzing dehydrogenation of the ChsH3 22-HOCO-CoA product and does not catalyze dehydrogenation of the EchA19 22-HOCO-CoA product. The results presented highlight the unique assembly of β-oxidation enzymes that Mtb utilizes to metabolize sterol side chains. The discovery of stereospecific ChsH3 and EchA19 enzymes that utilize the same substrate indicate a new branch of the cholesterol side-chain degradation pathway that may extend beyond core β-oxidation catabolic reactions (Scheme 1).

RESULTS

Through bioinformatic analyses, *chsB1* is the only gene in the KstR1 regulon that is annotated to encode a short-chain type alcohol dehydrogenase/reductase (SDR) or a 17-β-hydroxysteroid dehydrogenase, and *chsH3* is the last uncharacterized hydratase encoded in the KstR1 regulon. Given their gene loci, common regulation, and bioinformatic annotations, we hypothesized that ChsB1 and ChsH3 are involved in the sterol side-chain degradation in Mtb. Therefore, we undertook biophysical, biochemical, and structural characterizations of these two proteins to elucidate the specific steps in Mtb sterol metabolism catalyzed by these enzymes.

ChsH3 Is a Dimeric Enoyl-CoA Hydratase and Preferentially Catalyzes the Hydration of the Five-Carbon Sterol Intermediate 3-OCDO-CoA. Construct *pchsH3* (Table S1) was expressed heterologously in *R. jostii* RHA1 to provide ChsH3, which was isolated by ion affinity chromatography (IMAC) and further purified by gel filtration (Figure S1). To determine the oligomeric state of the purified ChsH3 in solution state, we performed analytical ultracentrifugation (AUC) sedimentation velocity analysis. The molecular weight determined by AUC indicated that ChsH3 forms a homodimer in solution (Figure S2).

We then assayed ChsH3 for hydratase activity using different substrates: *trans*-2-octenoyl-CoA, 3-oxo-pregna-4,17-diene-20-carboxyl-CoA (3-OPDC-CoA), 3-OCDO-CoA, and 3-oxo-cholest-4,24-dien-26-oyl-CoA (3-OCDS-CoA) (Figures 1A and S3). The latter three cholesterol metabolites are the enoyl-CoA species from the three separate β-oxidation cycles in the proposed cholesterol side-chain degradation pathway. The hydration reactions were monitored spectrophotometrically, and the formation of the hydrated products was further

https://doi.org/10.1021/acsinfecdis.1c00069
ACS Infect. Dis. 2021, 7, 1739−1751

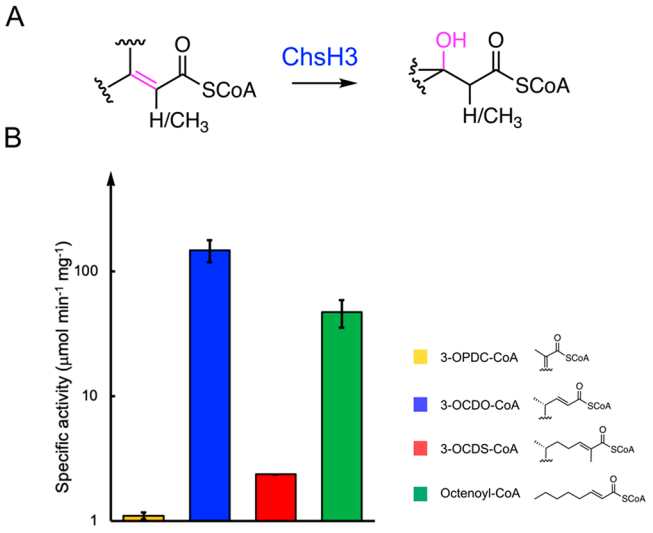

Figure 1. Specific activities of ChsH3 with enoyl-CoA substrates. (A) Reaction scheme for hydration catalyzed by ChsH3. (B) 3-OPDC-CoA, 3-OCDO-CoA, and 3-OCDS-CoA are the three-carbon, five-carbon, and eight-carbon enoyl-CoAs generated during cholesterol side-chain degradation. ChsH3 was assayed with 3-OPDC-CoA, 3-OCDO-CoA, 3-OCDS-CoA, and octenoyl-CoA at 50 μM. The specific activity was measured as the initial velocity of the first 10% of the hydration reaction. The specific activities are 1.1 ± 0.1, 147 ± 29, 2.40 ± 0.04, and 47.2 ± 12 μmol min^{-1} mg^{-1} for 3-OPDC-CoA, 3-OCDO-CoA, 3-OCDS-CoA, and octenoyl-CoA, respectively.

confirmed by matrix-assisted laser desorption ionization (MALDI) mass spectrometry. ChsH3 was able to bind and catalyze the hydration of bulky steroid enoyl-CoA esters as well as octenoyl-CoA, which is a medium-length fatty acyl ester. The highest activity was observed in the reactions with 3-OCDO-CoA (Figure 1B). ChsH3 also displayed high catalytic activity with octenoyl-CoA and modest activity with 3-OCDS-CoA (Figure 1B).

We then determined the steady-state kinetic rate constants for ChsH3 with 3-OCDO-CoA, octenoyl-CoA, and 3-OCDS-CoA as substrates. ChsH3 catalyzed the hydration of 3-OCDO-CoA most efficiently with an apparent second-order rate constant k_{cat}/K_m that is 15 times higher than for 3-OCDS-CoA and 1.3 times higher than for octenoyl-CoA (Table 1).

Table 1. Steady-State Kinetic Parameters for ChsH3 with Enoyl-CoA Thioesters

substrate	K_m (μM)	k_{cat} (s^{-1})	k_{cat}/K_m (M^{-1} s^{-1})
3-OCDO-CoA[a]	55 ± 5	113 ± 4	(2.0 ± 0.2) × 10^6
octenoyl-CoA[a]	112 ± 12	164 ± 8	(1.5 ± 0.2) × 10^6
3-OCDS-CoA[b]	12 ± 6	1.5 ± 0.7	(1.2 ± 0.1) × 10^5

[a]ChsH3 was assayed at 500 pM, pH 7.4, 25 °C. [b]ChsH3 was assayed at 5 nM, pH 7.4, 25 °C.

Thus, by examining the substrate specificity of ChsH3 with the enoyl-CoA thioesters of the cholesterol side-chain degradation intermediates and fatty enoyl-CoA, we established a role for ChsH3 in the second β-oxidation cycle of cholesterol side-chain catabolism in Mtb.

ChsH3 Is a MaoC-like Stereospecific Enoyl-CoA Hydratase. The amino acid sequence analysis of ChsH3 yields high similarity to the PLN-2864 enoyl-CoA hydratase superfamily. This superfamily of proteins consists of a C-terminal hot-dog fold, a characteristic of the MaoC domain, which is known to preferentially catalyze the hydration of 2-enoyl-CoA esters in a stereospecific manner.[16] In addition, sequence alignment of ChsH3 with other MaoC-like hydratases across species revealed the conserved active site residues Asp189 and His194 are present in ChsH3 (Figure S4).

We previously reported that EchA19 is an enoyl-CoA hydratase that is regulated by the KstR1 repressor and has been implicated in the cholesterol side-chain catabolism in Mtb, where it preferentially catalyzes the hydration of 3-OCDO-CoA among other sterol enoyl-CoA esters.[17] EchA19, structurally unlike ChsH3, possesses a canonical crotonase-like structure and is a member of the crotonase (PRK-07799) superfamily, which is known to catalyze the hydration of enoyl-CoAs with an opposite stereochemistry to the MaoC-like family.

To further investigate the role of ChsH3 and EchA19 in the cholesterol side-chain degradation pathway and the validity of their functional assignments, we characterized and compared the enzymatic products of the MaoC-like ChsH3 with the products of the crotonase EchA19. Analysis of the purified products of both enzymatic reactions by MALDI mass spectroscopy confirmed that both EchA19 and ChsH3 performed the hydration reaction on 3-OCDO-CoA, resulting in a product that was 18 Da greater than the starting material, 1136.37 (m-H/z) from 1118.36 (m-H/z) (Figure 2B).

The purified products from the individual reactions were lyophilized and subsequently subjected to nuclear magnetic resonance (NMR) spectroscopic analysis. ^{1}H NMR experiments were carried out in deuterium oxide. Analysis of spectra from 3-OCDO-CoA and 22-HOCO-CoA from EchA19 and ChsH3 showed the disappearance of olefinic peaks from the δ 5−6.5 ppm region and the appearance of three new protons in the δ 2.5−4.5 ppm region, which correspond to protons on C22 and C23 (Figure 2A), β and α to the thioester, respectively (Figure 2C). Comparison of the ^{1}H NMR spectra of the resulting 22-HOCO-CoA from ChsH3 and EchA19 confirmed that the two molecules were in fact configurationally different.

A 2D ^{1}H−^{1}H correlation spectroscopy (COSY) experiment was then carried out in order to assign the relevant peaks, and J coupling constants were determined to assign stereochemical configuration. The configuration at the C20 position (γ-carbon) is S in cholesterol and the conformation between C17 and C20 is essentially locked due to a high rotational barrier (Figure 2A). Thus, the dihedral angle between the γ and β protons that determines the J coupling constant is not rotationally averaged, and the J coupling may be used to determine the absolute configuration of each diastereomer. The γ and β J coupling constants were determined to be 1.3 ± 1 Hz for the ChsH3 product and 10.2 ± 1 Hz for the EchA19 product. Staggered γ−β Newman projections for the lowest energy conformer for each stereoisomer reveal a larger dihedral angle for the γ−β protons in the 22R-product, near 180°, vs 60° for the 22S-product. In accordance with the Karplus equation, the 22R-product is predicted to have a larger J coupling constant (Figure 2D), whereas the 22S-product is anticipated to have a smaller J coupling constant. Comparison to the ^{1}H NMR spectra of the enzymatic products revealed that ChsH3 produces (22S)-HOCO-CoA, and EchA19 produces (22R)-HOCO-CoA. These findings confirmed the stereochemical assignment of each enzymatic product from

https://doi.org/10.1021/acsinfecdis.1c00069
ACS Infect. Dis. 2021, 7, 1739−1751

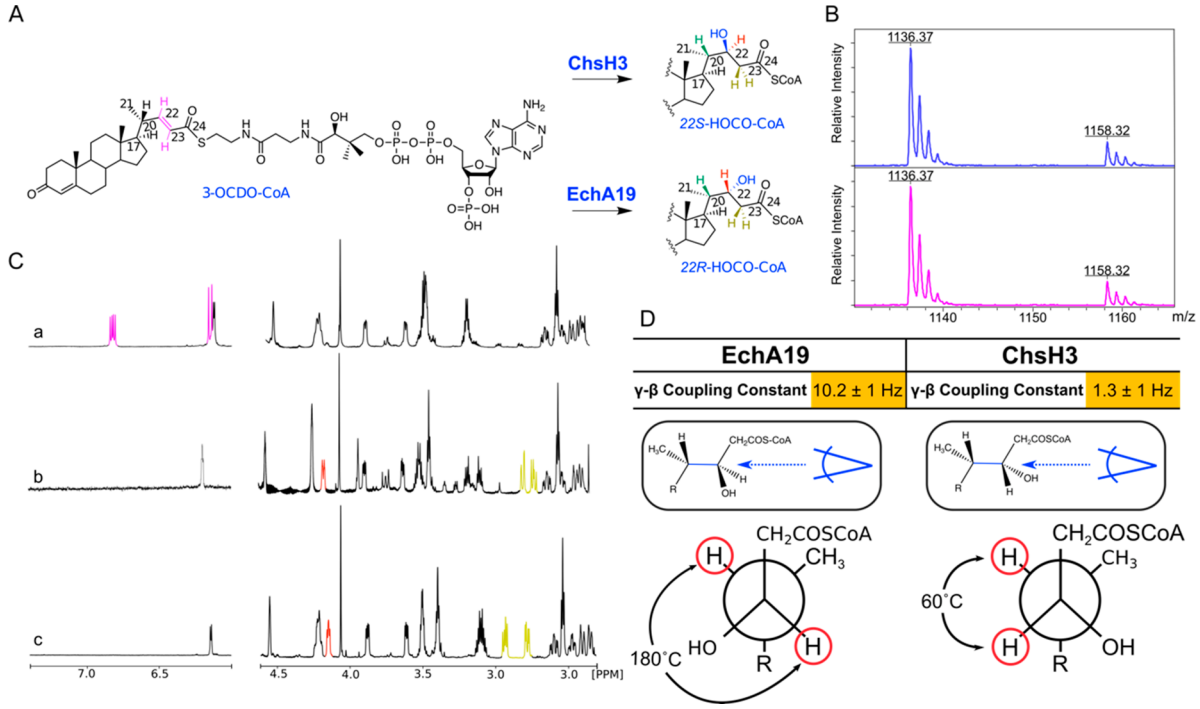

Figure 2. Analytical chemical characterizations of the hydration products from 3-OCDO-CoA catalyzed by ChsH3 or EchA19. (A) ChsH3 and EchA19 produce hydration products with different stereochemistry. (B) MALDI spectra of isolated hydration products of ChsH3 (blue) and EchA19 (pink) with 3-OCDO-CoA. $[M - H]^-$ = 1136.37 *m*/*z*, $[M + Na - 2H]^-$ = 1158.32 *m*/*z*. (C) ^{1}H NMR spectra of isolated (5 mM) (a) 3-OCDO-CoA, (b) (22*R*)-HOCO-CoA, and (c) (22*S*)-HOCO-CoA. Olefinic protons are colored pink, the C22 proton is colored red, and C23 protons are labeled in yellow. (D) *J* coupling constants between the C20 and C22 protons were used to estimate the H20−C20−C22−H22 dihedral angle and to determine the absolute configuration of the products of the EchA19 and ChsH3 hydration reactions. Staggered, lowest-energy-conformer Newman projections along the C20−C22 bond are depicted.

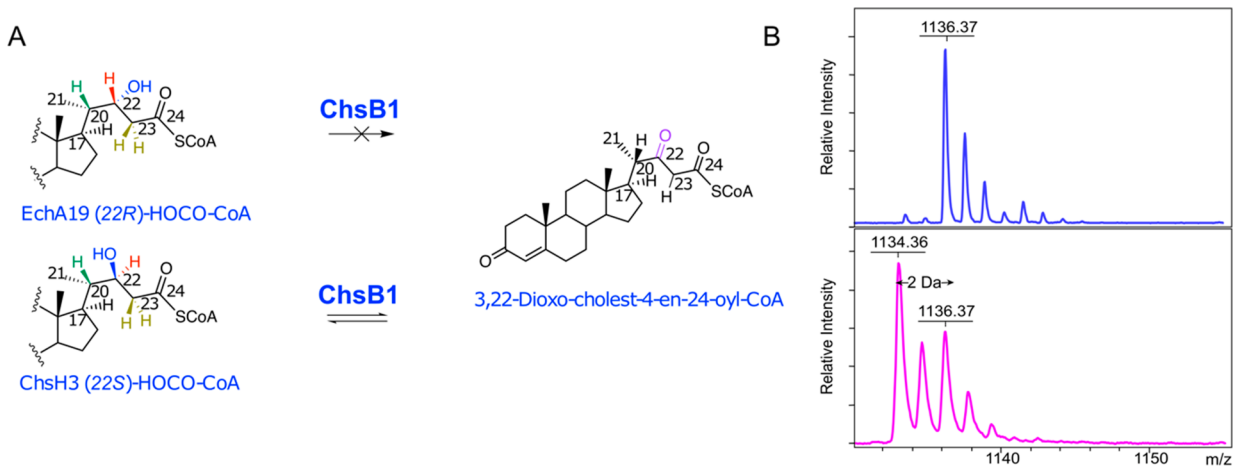

Figure 3. ChsB1 dehydrogenation reaction and compatibility with diastereomeric substrates. (A) Stereospecificity of the ChsB1-catalyzed dehydrogenation reaction. (B) MALDI spectra of the ChsB1-catalyzed dehydrogenation reactions using ChsH3-produced (pink) and EchA19-produced (blue) 22-HOCO-CoA as the substrate, $[M - H]^-$ = 1136.37 *m*/*z*.

ChsH3 and EchA19 and suggested different roles of each enzyme in the metabolism of the cholesterol side chain in Mtb.

The identical substrate specificity but opposite stereospecificity of ChsH3 and EchA19 prompted us to assess whether these two proteins also exist across steroid-utilizing actinobacteria. Through BLAST, we queried the protein sequences of ChsH3 and EchA19 against the nonredundant protein sequence database. We found that all the organisms belonging to Corynebacterineae under Actinobacteria, which possess homologues of ChsH3 with identities over 60%, have homologues of EchA19 with protein identities over 60% present as well (Figure S5) or vice versa. This observation indicates that the existence of stereochemistry-driven divergence in the steroid degradation pathway is likely to be conserved across the actinobacteria.

ChsB1 Is a Stereospecific Hydroxyacyl-CoA Dehydrogenase That Preferentially Catalyzes the Dehydrogenation of a Hydroxyl Cholesterol CoA Ester Metabolic Intermediate. Construct *pchsB1* (Table S1) was expressed heterologously in *R. jostii* RHA1 to provide ChsB1, which was

https://doi.org/10.1021/acsinfecdis.1c00069
ACS Infect. Dis. 2021, 7, 1739−1751

Table 2. Steady-State Kinetic Parameters for ChsB1[a]

	K_m (μM)		k_{cat} (s^{-1})	k_{cat}/K_m (M^{-1} s^{-1})
substrate	*hydroxyl substrate*	*NAD$^+$*		*hydroxyl substrate*
(22*S*)-HOCO-CoA[b]	5.3 ± 1	70 ± 10	9.0 ± 0.4	(1.7 ± 0.2) × 10^6
(22*R*)-HOCO-CoA[c]	NR[d]	NR	NR	NR
(3*R*)-hydroxyoctanoyl-CoA	169 ± 21[e]	162 ± 18[f]	2.5 ± 0.1[e]	(1.5 ± 0.2) × 10^4[e]
17β-hydroxyandrost-4-en-3-one	369 ± 75[g]	99 ± 9[h]	0.30 ± 0.03[g]	(8.1 ± 2) × 10^2[g]
17α-hydroxyandrost-4-en-3-one[i]	NR	NR	NR	NR
	K_m (μM)		k_{cat} (s^{-1})	k_{cat}/K_m (M^{-1} s^{-1})
substrate	*ketoester substrate*	*NADH*		*ketoester substrate*
3,22-dioxo-cholest-4-en-24-oyl-CoA	25 ± 5[j]	40 ± 6[k]	1.6 ± 0.2[j]	(6.4 ± 0.1) × 10^4[j]

[a]ChsB1 was assayed at pH 8.5, 25 °C. See Methods for enzyme concentrations. [b]Assayed varying both substrates, and data are fit globally to the bibi compulsory ordered mechanism. See Methods. [c]Assayed 50 μM (22*R*)-HOCO-CoA and 1 mM NAD$^+$ with 100 nM ChsB1. [d]NR: no reaction. [e]Assayed at a fixed [NAD$^+$] = 1 mM and fit to the Michaelis−Menten equation. [f]Assayed at a fixed [(3*R*)-hydroxyoctanoyl-CoA] = 350 μM and fit to the Michaelis−Menten equation. [g]Assayed at a fixed [NAD$^+$] = 1 mM and fit to the Michaelis−Menten equation. [h]Assayed at a fixed [17β-hydroxyandrost-4-en-3-one] = 800 μM and fit to the Michaelis−Menten equation. [i]Assayed [17α-hydroxyandrost-4-en-3-one] = 100 μM and [NAD$^+$] = 1 mM with 1 μM ChsB1. [j]Assayed at a fixed [NADH] = 1 mM and fit to the Michaelis−Menten equation. [k]Assayed at a fixed [3,22-dioxo-cholest-4-en-24-oyl-CoA] = 40 μM and fit to the Michaelis−Menten equation.

isolated by IMAC and further purified by gel filtration (Figure S1). AUC sedimentation velocity analysis was performed to determine the oligomeric state of ChsB1 in solution. The result indicated a homodimeric quaternary structure of ChsB1 in solution (Figure S2).

Protein sequence analysis of ChsB1 revealed that ChsB1 shared homologies with the hydroxyacyl-CoA dehydrogenases in the multifunctional enzyme type-2 (MFE-2) family from yeast and mammals.[18,19] Typically, these enzymes are hydroxyacyl-CoA dehydrogenases (HAD) with stereospecificity for the fatty acyl *R* diastereomer. To characterize the biochemical function of ChsB1, the recombinant protein was assayed for dehydrogenase activity using NAD$^+$ as the cofactor. Each 22-HOCO-CoA diastereomer, isolated from ChsH3 and EchA19 reactions, was individually tested as the substrate. The reactions were monitored spectrophotometrically. The formation of NADH at 340 nm was only observed when (22*S*)-HOCO-CoA from the ChsH3-catalyzed reaction was used as the substrate (Figure 3A). No activity was detected for 50 μM (22*R*)-HOCO-CoA (from EchA19) using 100 nM ChsB1 and 1 mM NAD$^+$. This selectivity was also confirmed by the mass shift of −2 Da in the MALDI mass spectrum of (22*S*)-HOCO-CoA, while the EchA19 product, (22*R*)- HOCO-CoA, was not oxidized (Figure 3B). When NADP$^+$ was assayed as the cofactor with (22*S*)-HOCO-CoA at 50 μM, minimal activity was observed for ChsB1, indicating ChsB1 utilizes NAD$^+$ as its cofactor.

As ChsB1 was also annotated as a 17β-hydroxysteroid dehydrogenase, we then spectroscopically examined its activity against 17β-hydroxyandrost-4-en-3-one and 17α-hydroxyandrost-4-en-3-one (chemical structures are shown in Figure S3). The concomitant formation of NADH was only observed with 17β-hydroxyandrost-4-en-3-one but not 17α-hydroxyandrost-4-en-3-one.

In order to elucidate the substrate preference, we determined the apparent steady-state rate constants for ChsB1 with (22*S*)-HOCO-CoA, (3*R*)-hydroxyoctanoyl-CoA, and 17β-hydroxyandrost-4-en-3-one by varying one substrate at a fixed saturating concentration of the second substrate. ChsB1 showed a high substrate preference toward (22*S*)-HOCO-CoA with an apparent second-order rate constant k_{cat}/K_m that is 100 times higher than for (3*R*)-hydroxyoctanoyl-CoA. Although ChsB1 was able to catalyze the dehydrogenation of 17β-hydroxyandrost-4-en-3-one, the k_{cat}/K_m is more than 3 orders of magnitude lower than for (22*S*)-HOCO-CoA (Table 2). We next determined the bibi reaction kinetic mechanism of ChsB1 by measuring initial velocities at varying concentrations of (22*S*)-HOCO-CoA and NAD$^+$ and determining the best global fit of the initial velocities based on the coefficient of determination (R^2) values. (Figure S6). The steady-state kinetics of ChsB1 with (22*S*)-HOCO-CoA and NAD$^+$ followed a compulsory ordered bibi mechanism with NAD$^+$ binding first. Catalysis can then occur via hydride transfer from the steroid substrate to the cofactor, after which, the ketoester is expected to dissociate from the ternary complex followed by release of NADH from the enzyme as has been observed in other SDRs.[20] With such a high catalytic efficiency, it is evident that ChsB1 functions as a sterol hydroxyacyl-CoA dehydrogenase in cholesterol side-chain degradation in Mtb.

To further characterize the reactivity of ChsB1, we assayed the reverse 3-keto reductase activity using NADH as the cofactor, and ChsB1 was able to catalyze the reduction of 3,22-dioxo-cholest-4-en-24-oyl-CoA. As compared spectrophotometrically, for the reverse reaction, the apparent k_{cat}/K_m is (6.3 ± 0.1) × 10^4 M^{-1} s^{-1} for 3,22-dioxo-cholest-4-en-24-oyl-CoA (Table 2).

ChsB1 Crystallizes as a Homodimer with a Classic Rossmann-Fold Motif but with a Larger Substrate Binding Cavity than Homologues. Needle-like ChsB1 crystals were obtained using the hanging drop vapor diffusion method. The structure was solved using the molecular replacement method and refined to a resolution of 2.03 Å (Table 3). The apo-structure of ChsB1 revealed a homodimeric structure within a single asymmetric unit (Figure 4A). Ample electron density allowed the structure to be built out, and 539/634 (85%) amino acids of the dimeric structure were modeled. The substrate binding loop, residues 217 to 230, which is known to be variable among HADs in order to accommodate a wide range of substrates accepted by SDR proteins, was the only intraprotein section that was not explicitly modeled due to a high degree of flexibility of this loop, while the remaining absent residues were N- and C-terminal.

The overall architecture of ChsB1 resembles its SDR homologues across a variety of organisms including yeast,

https://doi.org/10.1021/acsinfecdis.1c00069
ACS Infect. Dis. 2021, 7, 1739−1751

Table 3. Data Collection and Refinement Statistics

	ChsB1	ChsB1:NAD$^+$
data collection		
space group	*P* 21 21 21	*C*2
unit cell dimensions		
a, *b*, *c* (Å)	44.85, 80.13, 163.53	84.66, 84.23, 47.34
α, *β*, *γ* (deg)	90.00, 90.00, 90.00	90.00, 116.19, 90.00
diffraction limits (Å)[a]	2.00, 2.74, 2.52	
eigenvector-1[b]	1.00, 0.00, 0.00	
eigenvector-2[b]	0.00, 1.00, 0.00	
eigenvector-3[b]	0.00, 0.00, 1.00	
wavelength	0.9793	0.9793
resolution (Å)	81.77−2.03 (2.31−2.03)[c]	42.48−2.21 (2.25−2.21)[c]
R_{merge} (%)	0.20 (1.13)	0.15 (0.78)
$CC_{1/2}$	0.991 (0.665)	0.995 (0.739)
$I/\sigma I$	6.8 (1.8)	9.4 (2.3)
completeness (%)	93.1 (68.7)	100.0 (100.0)
redundancy	5.5 (6.1)	6.9 (5.6)
refinement		
resolution (Å)	81.77−2.03	42.12−2.21
no. reflections	122 908	103 397
R_{work}/R_{free}	21.20/24.99	16.70/20.89
Ramachandran analysis		
favored (%)	95.66	96.38
allowed (%)	4.34	3.62
outliers (%)	0	0
PDB ID	7LG9	7LGB

[a]Data were processed using anisotropic resolution limits. [b]The ellipsoidal diffraction limits and eigenvectors of the overall anisotropy tensor are indicated as direction cosines in the standard PDB orthogonal basis. [c]Values in parentheses are for the highest-resolution shell.

fungus, and mammal, as evidenced by the two-tandem repeat *β*/*α* Rossmann fold, in which a *β*-sheet is situated in between two sets of *α*-helices—typical of nucleoside cofactor binding proteins (Figure 4B). Interestingly, the Rossmann fold of ChsB1 and homologous HADs are different than the typical Rossmann motif, which maintains only six parallel *β*-strands in the distinct order of *β*3−*β*2−*β*1−*β*4−*β*5−*β*6 (Figure 4B). ChsB1 and homologues consist of a central *β*-sheet with two additional C-terminal *β*-strands, *β*7 and *β*8, and one additional *β*9/*α*11 repeat motif (Figure 4B). The *β*9/*α*11 repeat motif is extended outward, and *β*9 is incorporated into the *β*-sheet of the second monomer of the dimeric structure, while *α*11 interacts with *α*10 of the second monomer via van der Waals interactions between *α*11-(2) Ser243 and *α*10-(1) Pro289 as well as *α*11-(2) Phe247 and *α*10-(1) Thr293 and Leu296 (Figure S7). This conserved structural characteristic of the SDR family HADs contributes to the overall quaternary structure by providing an almost knot-like interface between individual monomers. The two largest helices, *α*7 and *α*9, which are parallel, form the dimeric interfacial region and consist of the largest surface area contact between monomers (Figure 4B). The orientation of the two monomers in relation to one another can be described by a mirror plane reflection followed by 180° rotation, resulting in the two sets of *α*7 and *α*9 helices having an antiparallel interaction. The geometric transformations of the monomers place the active sites on opposite sides of the structure, enabling catalytic activity on two faces.

The characteristic catalytic triad of SDRs, [His132]−Ser168−Tyr181−Lys185, is conserved in ChsB1 (Figure S8) and is spatially adjacent to the Gly−X−Gly−X−X−Ala NAD$^+$ cofactor binding motif[22] found in the loop between *α*1 and *β*1 (Figure 4B,C). Sequence alignment shows high conservation of residues across the main structural features, *β*-strands and *α*-helices, among ChsB1 and its HAD homologues (Figures S8 and S9). The greatest source of amino acid identity variability exists in the substrate binding loop and the final motifs, *β*9 and *α*11, which play a large role in the monomer−monomer interface and greatly contribute to the variability that is observed in the quaternary structure of the HAD homologues (Figure S9). The protein surface forms a large groove around the active sites, of nearly 30 Å, that leads into a slightly deeper cavity, nearly 10 Å deep where the catalytic residues lie. In comparison to its homologues, whose substrate binding cavities vary greatly in their dimensions, the binding groove of ChsB1 is of greater length and is largely exposed—likely to accommodate bulky [sterol-type] substrates. Structural alignment of ChsB1 and its homologues revealed that, although the NAD$^+$ binding sites are largely conserved, the length of the substrate binding pocket is linked to the length of the *β*8 strand regardless of the identity of the individual residues and their order (Figure S9). Across species, the length of the substrate binding pocket had an inverse relationship with the number of residues in the *β*8 strand; ChsB1 *β*8 for example contains five residues and had the longest substrate binding pocket length at around 30 Å, while its human homologue (PDB: 1ZBQ) contained nine residues and had a substantially shorter substrate binding pocket length at nearly 23 Å.

ChsB1 Forms a Complex with NAD$^+$ Cofactor. Co-crystallization of NAD$^+$ and ChsB1 yielded cubic crystals by sitting drop vapor diffusion that diffracted to a resolution of 2.21 Å (Table 3). Molecular replacement was used to solve the cocrystal structure using the apo-protein structure as the template. Each monomer of the homodimer of ChsB1/NAD$^+$ represents an asymmetric unit. The missing residues from 218 to 223 within the substrate binding domain in the apo-protein have been successfully modeled in the cocrystal structure. The substrate binding domain forms a short *α*-helix, *α*9′, between *β*6 and *α*10, which wraps on top of the Rossmann-fold motif to close the lid for binding NAD$^+$ (Figure 5A). Residues 68 to 70 were missing in the holo-protein structure; thus, the *α*4 helix is missing from the structure (Figure 5A). In addition, *β*9 in the apo-structure is replaced by a flexible loop in the holo-protein structure (Figure 5A).

The NAD$^+$ cofactor occupies two conformations in the binding site (Figure 5B,C), which is likely due to the high flexibility of the molecule caused by the absence of the hydroxyacyl-CoA ester substrate in the binding pocket. Conformation A is the predominant conformation. The binding of NAD$^+$ did not result in a large quaternary structural change. The ligand is bound between two surfaces, *α*3−*α*1−*α*10 and *α*5−*α*7−*α*9, and is in apposition to the *β*1−*β*4−*β*5−*β*6 sheet. The adenine−ribose moieties of the two NAD$^+$ conformations are almost identical, while the diphosphate moieties differ from each other—conformation A points toward *α*1, and conformation B points away (Figure 5B,C). The adenine nucleotides of the two NAD$^+$ conformations are in an anticonformation, and the ribose rings are in the C_2'-endo puckering conformation (Figure 5B,C). The active triad residues are located close to the nicotinamide moiety of NAD$^+$ (Figure 5B). In conformation A,

https://doi.org/10.1021/acsinfecdis.1c00069
ACS Infect. Dis. 2021, 7, 1739−1751

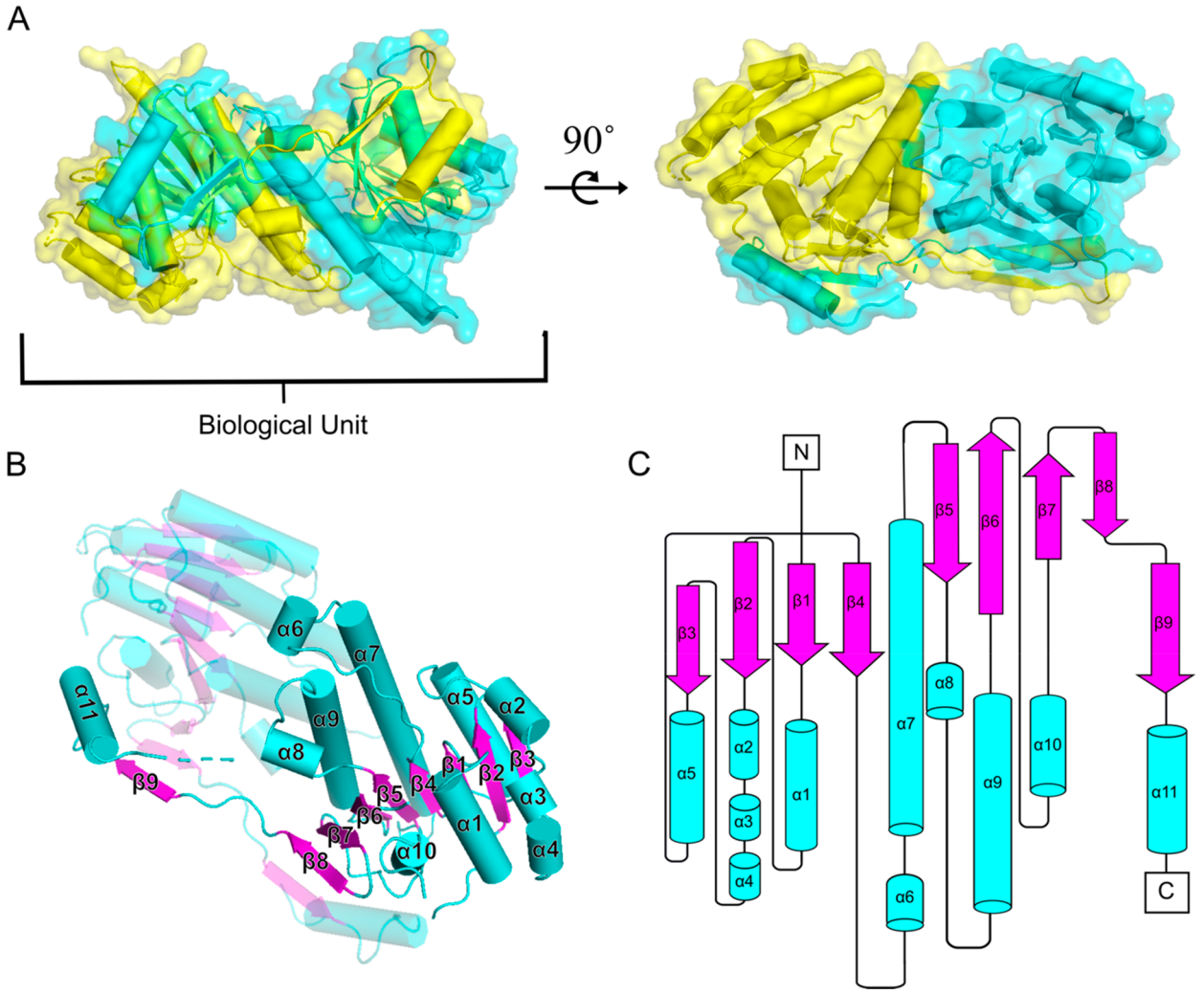

Figure 4. Overall atomic presentation of ChsB1. (A) The biologically functional unit is a homodimer with two active sites. (B) Each monomer is shown as cylindrical cartoons and colored by secondary structures with the identities of chains labeled. (C) Topology of one monomer is presented in the same color coding in panel B. The secondary structure was assigned using Pro-Origami.[21]

the nicotinamide amide moiety is pointing toward the active sites, while in conformation B, the amide is facing away.

Hydrogen bonding interactions (3 Å cutoff) between NAD^+ and the binding pocket residues were analyzed (Figure 5D). The adenine has strong hydrogen bonding interactions with the side chain of Asp82 and the backbone of Ile83. The nicotinamide ribose moiety in conformation A is in close contact with the catalytic triad residues with Lys185 and Tyr181 forming hydrogen bonds with the O4 and O3 hydroxyl groups and Ser168 forming a hydrogen bond with the amino group. In contrast, in conformation B, only Tyr181 is within 3 Å with the O3 hydroxyl groups of the ribose.

Protein sequence analysis by CoABind[23] identified distinct CoA binding residues/motifs in ChsB1. The predicted CoA binding residues mainly reside in the flexible loops between β4 and α6 and between α8 and α9 (Figure S10). An acetoacetyl-CoA was modeled into the structure of ChsB1 with NAD^+ based on a cocrystal structure of a ChsB1 homologue (PDB: 4N5M) (Figure S10). The CoA motif in the ligand matches well with the CoA binding residues predicted by CoABind. This observation further validates the utilization of a hydroxyacyl-CoA substrate in the reaction catalyzed by ChsB1.

DISCUSSION

The cholesterol degradation pathway in sterol-utilizing actinomycetes bifurcates at multiple stages through catalysis of duplicative chemistry with different stereochemical outcomes. In the terminal C26 oxidation of cholest-4-en-3-one, Cyp142 and Cyp125 both catalyze stereospecific terminal C26 oxidation, and their products are diastereomers of cholest-4-en-3-one-27-oic acid with opposite stereochemistry at C25 (Scheme 2).[24,25]

In the first cycle of side-chain β-oxidation, ChsE4−ChsE5 is stereospecific and catalyzes the dehydrogenation of (25*S*)-3-OCS-CoA.[26,27] A methyl acyl-CoA racemase, MCR, catalyzes epimerization of the C25 diastereomers of 3-OCS-CoA, which allows metabolic flux of both diastereomers into the cholesterol catabolic pathway (Scheme 2). Alternative fates of the (25*R*)-3-OCS-CoA are unknown.

In the second β-oxidation cycle, ChsE3 catalyzes dehydrogenation of 3-oxo-cholest-4-en-24-oyl-CoA (3-OCO-CoA) to 3-OCDO-CoA (Scheme 2).[26] Here, we demonstrate that ChsH3 catalyzes the hydration of 3-OCDO-CoA to form (22*S*)-HOCO-CoA. ChsB1 catalyzes the oxidation of the (22*S*)-HOCO-CoA to form a ketoacyl-CoA ester. FadA5 catalyzes the retro-Claisen cleavage of the five-carbon ketoacyl-

https://doi.org/10.1021/acsinfecdis.1c00069
ACS Infect. Dis. 2021, 7, 1739−1751

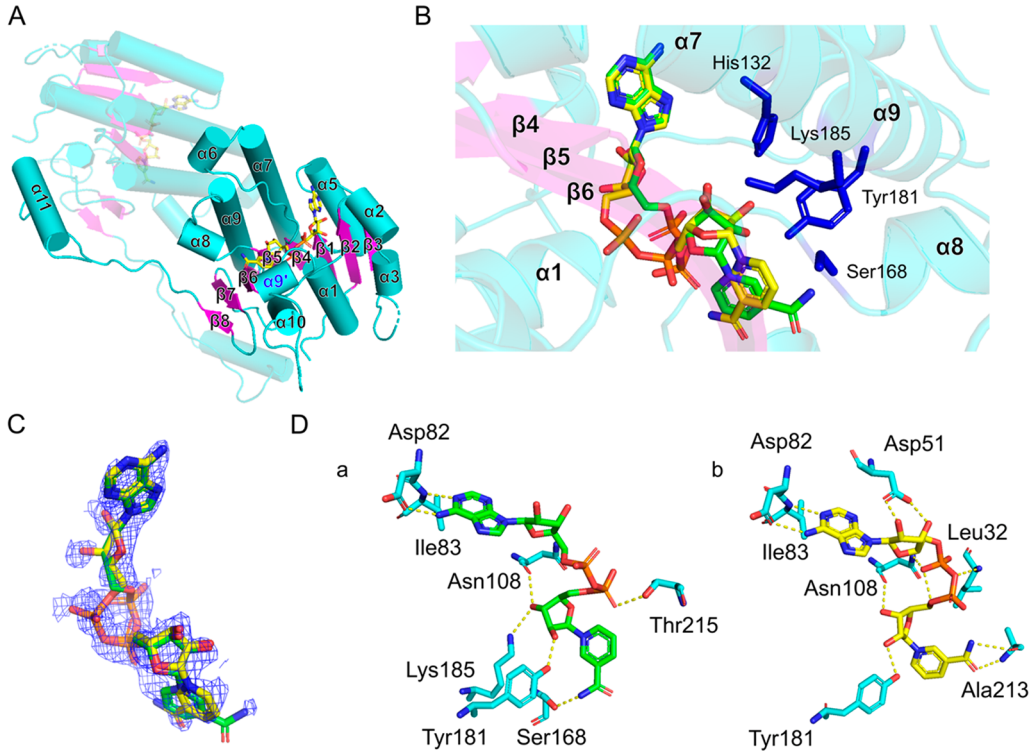

Figure 5. ChsB1 complexed with NAD^+. (A) Each monomer of ChsB1 has one substrate binding site. The homodimer is shown as cylindrical cartoons and colored by secondary structures with the identities of chains labeled. The missing substrate binding domain residue 218−223 in the apo-protein structure is labeled with $\alpha 9'$. NAD^+ is rendered as sticks and colored by atom. (B) Two conformations of NAD^+ were observed. Conformation A (green) is the predominant conformation, and conformation B is yellow. The catalytic triad residues and His132 are shown as blue sticks. (C) Electron density around NAD^+ is shown. A simulated annealing F_o-F_c omit map of NAD^+ contoured at 2.5σ was calculated to reduce the effects of model bias. NAD^+ conformation A is shown in green, and conformation B is shown in yellow. (D) Hydrogen bonding interactions (3 Å cutoff) between NAD^+ and ChsB1 are presented. Conformation A of NAD^+ is labeled green, and conformation B is labeled yellow.

CoA ester intermediate, 3,22-dioxo-cholest-4-en-24-oyl-CoA, to produce a three-carbon acyl-CoA ester cholesterol metabolite, 3-oxo-4-pregnene-2-carboxyl-CoA, and an acetyl-CoA (Scheme 2).[28]

Previously, we demonstrated that EchA19 preferentially catalyzes the hydration of 3-OCDO-CoA compared to the other enoyl-CoA intermediates of cholesterol side-chain catabolism.[17] Here, we find that the stereochemical outcome of the EchA19-catalyzed hydration is opposite to that of ChsH3, and (22*R*)-HOCO-CoA is produced.

Prior to our work, Xu et al. proposed that the *M. neoaurum* orthologue of *chsB1* (Rv3502c) encodes the 3-hydroxyacyl-CoA dehydrogenase in the second *β*-oxidation cycle of cholesterol side-chain degradation, although catalytic activity with the 22-HOCO-CoA substrate was not tested biochemically.[29] Deletion of the *chsB1* orthologue in mutant strain *M. neoaurum* ATCC 25795 (which also has impaired steroid ring degradation activity) results in accumulation of a three-carbon terminal hydroxyl cholesterol metabolite, 21-hydroxy-20-methylpregn-4-en-3-one (4-HBC), when the mutant is grown on cholesterol (Scheme 2).[29] Xu et al. proposed that the identity of the accumulated metabolite does not directly correlate to the substrate of the deleted 3-hydroxy acyl-CoA dehydrogenase and that the ChsB1 substrate is rerouted through an alternate metabolic pathway to form 4-HBC upon deletion of *chsB1*.

The 4-HBC metabolite from the *chsB1* knockout strain of *M. neoaurum* ATCC 25795 is likely to be accumulated only when the cholesterol ring degradation is deactivated. With equilibrium constants near 1, hydratase reactions are usually reversible under physiological substrate concentrations. Upon deletion of *chsB1,* the manifold of (22*S*)-HOCO-CoA conversion to keto-acyl-CoA will be blocked, and the flux of 3-OCDO-CoA will proceed through EchA19-mediated hydration of 3-OCDO-CoA. It is possible that the (22*R*)-HOCO-CoA produced by EchA19 could undergo carbon−carbon bond cleavage to form an aldehyde, 3-OPCA (Scheme 2), the formation of which can be coupled to a reductase to form the 21-hydroxy-20-methylpregn-4-en-3-one metabolite observed by Xu et al. in *M. neoaurum* ATCC 25795.[29] Retro-aldol cleavage to form a ketone product occurs in the last cycle of side-chain *β*-oxidation through Ltp2.[30,31] In addition, aldolytic reactions have been reported in cholate side-chain degradation in *Pseudomonas sp.* Chol1[32] and anaerobic cholesterol side-chain degradation in *Sterolibacterium denitrificans* Chol1S.[33,34]

Alternatively, coupling formation of 3-OPCA with a dehydrogenation to form 3-oxo-4-pregnadiene-20-carboxylic acid (Scheme 2) would aid formation of the thermodynamically unfavorable aldehyde from an aldolase reaction and prevent reaction of the 3-OPCA with nucleophiles in the cell. Subsequent ligation of CoA with 3-oxo-4-pregnadiene-20-carboxylic acid would rescue the metabolite and allow reentry into the cholesterol catabolism pathway. However, such a CoA ligase has not been identified in Mtb nor is there an annotated CoA transferase in the KstR1 regulon.[11] The Mtb genome does not contain an orthologue of *casI*, the 3-oxo-4-pregnadiene-20-carboxylic acid CoA ligase present in actinomycete *R. jostii* RHA1.[35]

https://doi.org/10.1021/acsinfecdis.1c00069
ACS Infect. Dis. 2021, 7, 1739−1751

Scheme 2. Stereochemical Bifurcations in Mtb Cholesterol Metabolism[a]

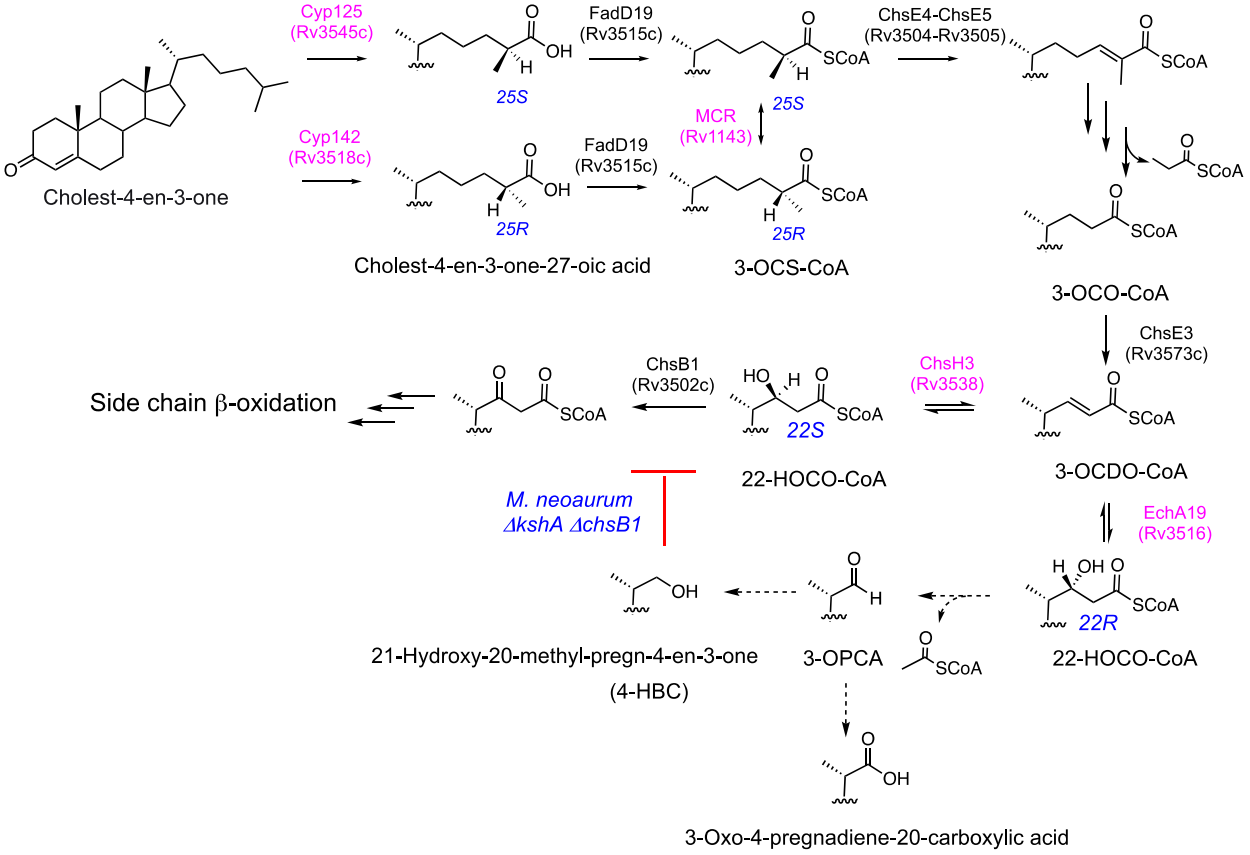

[a]ChsH3 and EchA19 are hydratases with identical substrate specificities that produce opposite product stereochemistry at C22. Cyp125 and Cyp142 are cytochrome P450 oxidases with identical substrate specificities that produce opposite product stereochemistry at C25.

Table 4. Gene Essentiality in Cholesterol Metabolism

	relative increase in transcription cholesterol/glycerol[a]	essentiality for growth on cholesterol[b]	essentiality for survival in mice[c]
echA19	5.23	nonessential	nonessential
chsH3	3.61	essential	nonessential
chsB1	4.46	essential	essential

[a]Transcription upregulation by cholesterol after 24 h.[15] [b]Required for in vitro growth in cholesterol media by transposon mapping.[36] [c]Required for growth in C57BL/6J mouse spleen, by transposon site hybridization (TraSH).[37]

chsH3 and *chsB1* are both required for Mtb growth on cholesterol (Table 4),[36] indicating the essential functions of these two genes and their gene products in cholesterol catabolism in Mtb. The resulting (22*R*)-HOCO-CoA from EchA19 is not a substrate of ChsB1, and *echA19* is not essential for growth on cholesterol.[36] These data suggest a different function than catabolic *β*-oxidation of cholesterol for this hydratase, a role that has yet to be fully elucidated.

Typically, in bacteria, one hydroxyacyl-CoA diastereomer is used in biosynthesis of polyesters for energy storage, and the other is used in fatty acid degradation for energy production. Genes encoding putative SCP-2 aldolases Ltp3 and Ltp4 are both highly upregulated in Mtb and *R. jostii* RHA1 during growth on cholesterol.[15,38] SCP-2 proteins have been shown to have multiple roles in lipid metabolism and intracellular lipid transfer. Typically, the N-terminus of an SCP-2 protein functions as a ketoacyl-CoA thiolase, and the C-terminus functions as the sterol carrier domain of the protein that can be proteolytically cleaved and is responsible for intracellular lipid transfer for cell wall or membrane biosynthesis.[39,40] It is possible that the EchA19-produced (22*R*)-HOCO-CoA could be transferred and cleaved through these sterol transfer proteins for construction or storage of other lipids.[41]

The EchA19-catalyzed hydration reaction is reversible, and we previously reported that EchA19 is regulated by succinylation through lysine post-translational modification.[17] Since the EchA19 product appears to be the nonproductive direction for cholesterol catabolism, a possible role for succinylation might be regulating the flow of cholesterol between catabolism and lipid utilization in the bacterium. ChsH3 and EchA19 are largely conserved in steroid-utilizing actinobacteria, indicating the general involvement of both hydroxyacyl-CoA diastereomers in the steroid degradation pathway in actinobacteria.

In this work, we elucidate a second example of stereochemical bifurcation in the cholesterol metabolism pathway in Mtb (Scheme 2). Throughout the cholesterol catabolic pathway, we have identified protein architectures and assemblies that are unique to actinomycetes and Mtb.[26,30,42−45] Importantly, *chsB1* is required for the in vivo survival of Mtb in mice,[37] and the structures of ChsB1 elucidated in this work provide insight into binding site cavities that differ from its homologues and will allow discrimination between host and pathogen enzymes by inhibitors in the

https://doi.org/10.1021/acsinfecdis.1c00069
ACS Infect. Dis. 2021, 7, 1739−1751

future. The enzymatic evolutionary adaptations that have emerged in Mtb for the breakdown of cholesterol and the in vivo essentiality of various genes in the pathway highlight the value of this pathway's enzymes for further exploitation in drug discovery.

METHODS

Materials, Strains, Media, and General Methods. Mtb H37Rv total genomic DNA was obtained from the TB Research Materials Facility at Colorado State University (NIAD NO1-AI40091). Coenzyme A and nicotinamide adenine dinucleotide (NAD, grade I, free acid) were purchased from MilliporeSigma (Burlington, MA). Testosterone was obtained from Steraloids Inc. (Newport, RI). Thiostrepton (*Streptomyces laurentii*) was purchased from Thermo Fisher Scientific (Ward Hill, MA). Chloramphenicol was from IBI Scientific (Dubuque, IA). Ampicillin was purchased from Roche Diagnostics (Indianapolis, IN). iProof DNA polymerase and IMAC nickel resin were from Bio-Rad (Hercules, CA). Restriction endonucleases, Quick Ligase, and the protein ladder were from New England Biolabs (Beverly, MA). Superdex 200 HiLoad 16/60 columns were from GE Healthcare Biosciences Corp. (Piscataway, NJ). ZipTip U−C18 was from Merck Millipore. Oligonucleotides were from Integrated DNA Technologies (Coralville, IA). Sanger DNA sequencing (performed by GENEWIZ LLC) was used to verify the coding sequence of the expression plasmids. All other chemicals were obtained from Fisher Scientific (Hampton, NH), unless otherwise stated. XL1-Blue *E. coli* was obtained from Agilent. The *R. jostii* RHA1 strain is a gift from Lindsay Eltis (Department of Microbiology and Immunology, University of British Columbia). The pTipQC1 vector is a gift from Tomohiro Tamura (National Institute of Advanced Industrial Science and Technology, Sapporo, Japan). The LB media is composed of 25 g of Luria broth. Buffer A: 20 mM Tris-HCl pH 8.5, 300 mM NaCl, and 10 mM imidazole. Buffer B: 20 mM Tris-HCl pH 8.5, 300 mM NaCl, and 500 mM imidazole. Buffer C: 50 mM Tris-HCl pH 8.5 and 200 mM NaCl. Buffer D: 100 mM HEPES-HCl pH 7.4 and 3 mM EDTA. Buffer E: 100 mM TAPS-HCl pH 8.5 and 150 mM NaCl.

Expression Plasmid Construction. *chsB1* and *chsH3* were amplified from Mtb H37Rv total genomic DNA by PCR (Table S1). The PCR products were digested with NdeI and *Hin*dIII restriction endonucleases and ligated into the pTipQC1 vector. Ligated plasmids containing the gene of interest were transformed into competent *E. coli* XL1-Blue cells for amplification and isolation of plasmid DNA. DNA sequencing of the plasmids confirmed that the sequences were correct and that no mutations were introduced during PCR amplification.

Protein Preparation Using Heterologous Expression in *R. jostii* RHA1. Construct *pchsB1* (Rv3502c) or *pchsH3* (Rv3538) was used for the expression of ChsB1 or ChsH3 in *R. jostii* RHA1 (Table S1). The appropriate plasmid was transformed into *R. jostii* RHA1 cells through electroporation. Single colonies were selected on LB plates containing 30 μg/mL chloramphenicol and cultured in LB media at 30 °C. Expression was induced at OD600 ≈ 0.4−0.6 by the addition of 20 μg/mL thiostrepton, and cells were grown at 30 °C for 24 h.

Cells were harvested by centrifugation at 5000 rpm for 20 min at 4 °C, and all subsequent steps were conducted at 4 °C. The cells were suspended in Buffer A and lysed by cell disruption (four passages at 27 000 psi). Cellular debris was removed by ultracentrifugation at 40 000 rpm (185 511*g*) for 1 h. The supernatant was loaded onto IMAC nickel resin, washed with 10 column volumes of Buffer A, and eluted with Buffer B. Protein solutions were immediately desalted by dialysis with Buffer C.

Isolated proteins in Buffer C were concentrated by ultrafiltration (MWCO 10 kDa) to less than 2 mL and purified by size-exclusion chromatography (SEC) on a Superdex 200 column equilibrated in Buffer C. The column was equilibrated in Buffer C at a flow rate of 1.0 mL/min and monitored at 280 nm. Fractions were collected and analyzed by reducing SDS-PAGE analysis. The fractions containing desired proteins were concentrated by ultrafiltration (MWCO 10 kDa).

Substrate Synthesis. 3-Oxo-pregna-4,17-diene-20-carboxyl-CoA (3-OPDC-CoA), 3-OCDO-CoA, 3-OCDS-CoA, and *trans*-2-octenoyl-CoA were synthesized as previously reported.[17] To make (22*R*)-HOCO-CoA or (3*R*)-hydroxyoctanoyl-CoA, 200 μM 3-OCDO-CoA or *trans*-2-octenoyl-CoA was incubated with 1 μM ChsH3 in buffer D in a 10 mL reaction volume at 25 °C for 2 h. The reaction was quenched by adding 100 μL of TFA and product was purified by HPLC on a C18 column using 10 mM ammonium acetate with a linear gradient of acetonitrile from 5 to 100% over 40 min. (22*S*)-HOCO-CoA was synthesized in a similar manner by using EchA19. The purities of the substrates were accessed by analytical HPLC to be over 99% pure.

The identity of the desired product was confirmed by MALDI mass spectrometry. Matrices for MALDI mass spectrometry were prepared by dissolving 2,5-dihydroxybenzoic acid (20 mg/mL) in a 7:3 (v/v) mixture of 0.1% (v/v) trifluoroacetic acid and acetonitrile. MALDI mass spectra were acquired on a Bruker Microflex operated in the reflectron negative mode. Mass spectral data were analyzed using Bruker flexAnalysis software (version 3.4).

NMR Spectroscopy Characterization of Reaction Products from ChsH3 and EchA19. Reaction products from ChsH3 and EchA19 using 3-OCDO-CoA as the substrate were purified by HPLC on a C18 column using 10 mM ammonium acetate with a linear gradient of acetonitrile from 5 to 100% over 40 min. The solvents were removed under reduced pressure followed by lyophilization. The resulting purified products were characterized on an 850 mHz Bruker Ascend spectrometer by dissolving the CoA esters in D_2O to a final concentration of 50 μM. Chemical shifts are reported in ppm (δ) calibrated using residual protic solvent as an internal reference.

Steady-State Kinetics. *Hydratase Assay.* ChsH3 was assayed for hydratase activity with substrates 3-OCDO-CoA, 3-OCDS-CoA, and octenoyl-CoA in buffer D containing 500 pM enzyme (5 nM for 3-OCDS-CoA) at 25 °C. Reactions were initiated by the addition of enzyme and were monitored at 263 nm. Product formation was quantified using $\varepsilon_{263\ nm}$ = 6700 M^{-1} cm^{-1}, which corresponds to the α,β-unsaturation of the enoyl-CoA substrates. Initial velocities were determined from the first 10% of the reaction. The rates of product formation were fit to the Michaelis−Menten equation to determine k_{cat} and K_M for each substrate. Each initial velocity was determined in triplicate, and at least five different substrate concentrations were examined. 3-OCDO-CoA ranged from 5 to 250 μM; 3-

https://doi.org/10.1021/acsinfecdis.1c00069
ACS Infect. Dis. 2021, 7, 1739−1751

OCDS-CoA ranged from 2.5 to 80 μM; octenoyl-CoA ranged from 5 to 300 μM.

Hydroxy Dehydrogenase Assay. ChsB1 was assayed for hydroxyl dehydrogenase activity with substrate (22*R*)-HOCO-CoA, (3*R*)-hydroxyoctanoyl-CoA, and testosterone in buffer E containing 5 nM enzyme for 20-HOCO-CoA, 300 nM enzyme for 3-hydroxyoctanoyl-CoA, and 1 μM for testosterone at 25 °C. For testosterone, the stock solution was prepared in ethanol (50 mM). No oxidation of ethanol was detected in control assays. The final volume of ethanol was kept constant in all assays at 5% (v/v). Assays were initiated by the addition of enzyme and were monitored at 340 nm for the reduction of NAD^+ to NADH. Product formation was quantified using $\varepsilon_{340\ nm}$ = 6300 M^{-1} cm^{-1}. Initial velocities were determined from the first 10% of the reaction and were obtained as a function of one of the substrates while keeping the second substrate at a fixed, saturating concentration. k_{cat} and K_M for each substrate were determined by fitting the initial velocities of product formation into the Michaelis−Menten equation. Each initial velocity was determined in triplicate, and at least five different substrate concentrations were examined. (22*R*)-HOCO-CoA ranged from 2.5 to 40 μM; (3*R*)-hydroxyoctanoyl-CoA ranged from 10 μM to 1 mM; testosterone ranged from 100 to 800 μM; NAD^+ ranged from 50 μM to 1 mM. To assess the bi-bi reaction kinetic mechanism of ChsB1, reaction velocities were measured by varying concentrations of (22*S*)-HOCO-CoA and at different fixed concentrations of NAD^+. The initial velocities were globally fit to different models and the best fit (based on R^2 value) was found to be to the following equation using GraphPad Prism8.

$$v = \frac{V_m[A][B]}{K_{iA}K_{mB} + K_{mB}[A] + K_{mA}[B] + [A][B]}$$

where K_{mA} and K_{mB} are the Michaelis constants for A and B at saturating concentrations of B and A, respectively, K_{iA} is the dissociation constant for the enzyme and A, and V_m is the maximum velocity of the reaction.

Analytical Ultracentrifugation. Sedimentation velocity AUC experiments were performed at 20 °C using a Beckman Coulter XL-I analytical ultracentrifuge with an An-60Ti rotor at 325 000 rpm for 12 h with scans performed every 60 s. A double-sector cell, equipped with a 12 mm Epon centerpiece and sapphire windows, was loaded with 380 and 400 μL of sample and buffer C, respectively. The concentrations that were used in the experiments are 31.8 μM for ChsB1 and 30 μM for ChsH3 in buffer C. Samples were monitored with UV at 280 nm. The data were analyzed with Sedfit version 1501b using a continuous c(s) distribution. Numerical values for the solvent density, viscosity, and the partial specific volume were determined using Sednterp. Residual and c(s) distribution graphs were plotted using GUSSI.

Protein Crystallization. The ChsB1 apo-protein crystals were obtained by hanging drop vapor diffusion at room temperature. Briefly, 2 μL of a 20 mg mL^{-1} protein was mixed 1:1 with a reservoir solution of 15% w/v polyethylene glycol 4000, 0.2 M ammonium acetate, and 0.1 M sodium citrate pH 5.6 and equilibrated against 500 μL of the reservoir solution. The crystals were then harvested and transferred to a cryoprotectant solution containing the mother liquor and 25% ethylene glycol. For ChsB1 cocrystallization, ChsB1 was mixed with NAD^+, and cocrystals were obtained by sitting drop vapor diffusion at room temperature. A 20 mg mL^{-1} concentration of protein was preincubated with NAD^+ (1:1.2 molar ratio) for 15 min on ice. A 200 nL aliquot of the mixture was then mixed 1:1 with the mother liquor, which contains 0.2 M sodium citrate, 0.1 M HEPES pH 7.5, and 30% v/v 2-methyl-2,4-pentanediol. Crystals were harvested and cryo-cooled in liquid nitrogen before data collection.

X-ray Data Collection and Structural Determination. Diffraction data were collected at the FMX beamline of the National Synchrotron Light Source-II at Brookhaven National Laboratory (Upton, NY) at the selenium absorption edge using a wavelength of 0.9793 Å. Data sets were processed using XDS[46] and Aimless[47] as implemented in the autoPROC pipeline.[48] Diffraction for the apo-protein crystals was strongly anisotropic and thus was further processed with STARANISO.[49] Phases were obtained by molecular replacement using Phaser. A search model for the apo-protein was created from 4KZP and the holo-protein model was created from the ChsB1 apo-protein model. Model building was carried out in Coot, followed by refinement in Phenix. The geometric quality of the refined model was assessed with MolProbity and the structure validation tools in the Phenix suite. Data collection and refinement statistics are shown in Table 3.

■ ASSOCIATED CONTENT

Supporting Information

The Supporting Information is available free of charge at https://pubs.acs.org/doi/10.1021/acsinfecdis.1c00069.

> Expression constructs, SDS-PAGE of ChsB1 and ChsH3, AUC analysis of ChsB1 and ChsH3, chemical structures for substates used in enzyme kinetics, protein sequence alignments, phylogenetic trees for ChsH3 or EchA19 and their homologues across Actinobacteria, ChsB1 kinetic plots, and additional structural analyses of ChsB1 (PDF)

Accession Codes

Atomic coordinates and structure factors for ChsB1 and ChsB1/NAD^+ have been deposited in the Protein Data Bank with accession codes 7LG9 and 7LGB. UniProt accession IDs for proteins used in this work: ChsH3, Q6MWW2; EchA19, O53561; ChsB1, O53547.

■ AUTHOR INFORMATION

Corresponding Author

Nicole S. Sampson − *Department of Chemistry, Stony Brook University, Stony Brook, New York 11794-3400, United States;* orcid.org/0000-0002-2835-7760; Phone: +1-631-632-7952; Email: nicole.sampson@stonybrook.edu; Fax: +1-631-632-5738

Authors

Tianao Yuan − *Department of Chemistry, Stony Brook University, Stony Brook, New York 11794-3400, United States;* orcid.org/0000-0002-4700-8654

Joshua M. Werman − *Department of Chemistry, Stony Brook University, Stony Brook, New York 11794-3400, United States;* orcid.org/0000-0002-8521-7369

Xingyu Yin − *Biochemistry and Structural Biology Graduate Program, Stony Brook University, Stony Brook, New York 11794-5215, United States;* orcid.org/0000-0003-3832-0547

Meng Yang − *Department of Chemistry, Stony Brook University, Stony Brook, New York 11794-3400, United States;* orcid.org/0000-0002-1371-5844

Miguel Garcia-Diaz − *Department of Pharmacological Sciences, Stony Brook University, Stony Brook, New York 11794-8651, United States;* orcid.org/0000-0003-1605-6861

Complete contact information is available at: https://pubs.acs.org/10.1021/acsinfecdis.1c00069

Author Contributions

[‖]T.Y., J.M.W., and X.Y.Y. contributed equally to this work.

Notes

The authors declare no competing financial interest.

■ ACKNOWLEDGMENTS

The X-ray experiments were conducted using resources of the National Synchrotron Light Source II, a U.S. Department of Energy (DOE) Office of Science User Facility operated for the DOE Office of Science by Brookhaven National Laboratory under contract no. DESC0012704. This research is funded by NIH RO1AI134054 to N.S.S. The authors would like to thank Dr. Kalle Gehring from McGill University for his help with AUC analysis. The authors also thank Dr. Lindsay Eltis from the University of British Columbia for providing *R. jostii* RHA1 and Dr. Tomohiro Tamura from the National Institute of Advanced Industrial Science and Technology (AIST), Japan, for providing the pTipQC1 vector.

■ ABBREVIATIONS

AUC, analytical ultracentrifugation; CoA, coenzyme A; HAD, hydroxyacyl-CoA dehydrogenase; 4-HBC, 21-hydroxy-20-methyl-preg-4-en-3-one; 22-HOCO-CoA, 22-hydroxy-3-oxo-cholest-4-en-24-oyl-CoA; IMAC, ion affinity chromatography; MALDI, matrix-assisted laser desorption ionization; MCR, methyl acyl-CoA racemase; Mtb, *Mycobacterium tuberculosis*; NAD^+, nicotinamide adenine dinucleotide; $NADP^+$, nicotinamide adenine dinucleotide phosphate; 3-OCDO-CoA, 3-oxo-chol-4,22-dien-24-oyl-CoA; 3-OCDS-CoA, 3-oxo-cholest-4,24-dien-26-oyl-CoA; 3-OPCA, 3-oxo-preg-4-en-21-carbaldehyde; 3-OPDC-CoA, 3-oxo-pregna-4,17-diene-20-carboxyl-CoA; *R. jostii* RHA1, *Rhodococcus jostii* RHA1; SDR, short-chain type alcohol dehydrogenase/reductase; TB, tuberculosis

■ REFERENCES

(1) World Health Organization. Global tuberculosis report 2020. https://apps.who.int/iris/bitstream/handle/10665/336069/9789240013131-eng.pdf (accessed 7 February 2021).

(2) Yuan, T., Werman, J. M., and Sampson, N. S. (2021) The pursuit of mechanism of action: uncovering drug complexity in TB drug discovery. *RSC Chemical Biology*.

(3) de Carvalho, L. P., Fischer, S. M., Marrero, J., Nathan, C., Ehrt, S., and Rhee, K. Y. (2010) Metabolomics of *Mycobacterium tuberculosis* reveals compartmentalized co-catabolism of carbon substrates. *Chem. Biol. 17*, 1122−1131.

(4) Zimmermann, M., Kogadeeva, M., Gengenbacher, M., McEwen, G., Mollenkopf, H. J., Zamboni, N., Kaufmann, S. H. E., and Sauer, U. (2017) Integration of metabolomics and transcriptomics reveals a complex diet of *Mycobacterium tuberculosis* during early macrophage infection. *mSystems 2*, e00057-17.

(5) Pandey, A. K., and Sassetti, C. M. (2008) Mycobacterial persistence requires the utilization of host cholesterol. *Proc. Natl. Acad. Sci. U. S. A. 105*, 4376−4380.

(6) Wilburn, K. M., Fieweger, R. A., and VanderVen, B. C. (2018) Cholesterol and fatty acids grease the wheels of *Mycobacterium tuberculosis* pathogenesis. *Pathog. Dis. 76*, fty021.

(7) Yuan, T., and Sampson, N. S. (2018) Hit generation in TB drug discovery: from genome to granuloma. *Chem. Rev. 118*, 1887−1916.

(8) Bonds, A. C., and Sampson, N. S. (2018) More than cholesterol catabolism: regulatory vulnerabilities in *Mycobacterium tuberculosis*. *Curr. Opin. Chem. Biol. 44*, 39−46.

(9) VanderVen, B. C., Fahey, R. J., Lee, W., Liu, Y., Abramovitch, R. B., Memmott, C., Crowe, A. M., Eltis, L. D., Perola, E., Deininger, D. D., Wang, T., Locher, C. P., and Russell, D. G. (2015) Novel inhibitors of cholesterol degradation in *Mycobacterium tuberculosis* reveal how the bacterium's metabolism is constrained by the intracellular environment. *PLoS Pathog. 11*, No. e1004679.

(10) Yang, X., Yuan, T., Ma, R., Chacko, K. I., Smith, M., Deikus, G., Sebra, R., Kasarskis, A., van Bakel, H., Franzblau, S. G., and Sampson, N. S. (2019) Mce3R stress-resistance pathway is vulnerable to small-molecule targeting that improves tuberculosis drug activities. *ACS Infect. Dis. 5*, 1239−1251.

(11) Wipperman, M. F., Sampson, N. S., and Thomas, S. T. (2014) Pathogen roid rage: cholesterol utilization by *Mycobacterium tuberculosis*. *Crit. Rev. Biochem. Mol. Biol. 49*, 269−293.

(12) Upton, A. M., and McKinney, J. D. (2007) Role of the methylcitrate cycle in propionate metabolism and detoxification in *Mycobacterium smegmatis*. *Microbiology (London, U. K.) 153*, 3973−3982.

(13) Savvi, S., Warner, D. F., Kana, B. D., McKinney, J. D., Mizrahi, V., and Dawes, S. S. (2008) Functional characterization of a vitamin B12-dependent methylmalonyl pathway in *Mycobacterium tuberculosis*: implications for propionate metabolism during growth on fatty acids. *J. Bacteriol. 190*, 3886−3895.

(14) Lee, W., VanderVen, B. C., Fahey, R. J., and Russell, D. G. (2013) Intracellular *Mycobacterium tuberculosis* exploits host-derived fatty acids to limit metabolic stress. *J. Biol. Chem. 288*, 6788−6800.

(15) Nesbitt, N. M., Yang, X., Fontan, P., Kolesnikova, I., Smith, I., Sampson, N. S., and Dubnau, E. (2010) A thiolase of *Mycobacterium tuberculosis* is required for virulence and production of androstenedione and androstadienedione from cholesterol. *Infect. Immun. 78*, 275−282.

(16) Park, S. J., and Lee, S. Y. (2003) Identification and characterization of a new enoyl coenzyme A hydratase involved in biosynthesis of medium-chain-length polyhydroxyalkanoates in recombinant *Escherichia coli*. *J. Bacteriol. 185*, 5391−5397.

(17) Bonds, A. C., Yuan, T., Werman, J. M., Jang, J., Lu, R., Nesbitt, N. M., Garcia-Diaz, M., and Sampson, N. S. (2020) Post-translational succinylation of *Mycobacterium tuberculosis* enoyl-CoA hydratase EchA19 slows catalytic hydration of cholesterol catabolite 3-oxo-chol-4,22-diene-24-oyl-CoA. *ACS Infect. Dis. 6*, 2214−2224.

(18) Haapalainen, A. M., Koski, M. K., Qin, Y. M., Hiltunen, J. K., and Glumoff, T. (2003) Binary structure of the two-domain (3R)-hydroxyacyl-CoA dehydrogenase from rat peroxisomal multifunctional enzyme type 2 at 2.38 A resolution. *Structure 11*, 87−97.

(19) Ylianttila, M. S., Pursiainen, N. V., Haapalainen, A. M., Juffer, A. H., Poirier, Y., Kalervo Hiltunen, J., and Glumoff, T. (2006) Crystal structure of yeast peroxisomal multifunctional enzyme: structural basis for substrate specificity of (3*R*)-hydroxyacyl-CoA dehydrogenase units. *J. Mol. Biol. 358*, 1286−1295.

(20) Benach, J., Atrian, S., Gonzalez-Duarte, R., and Ladenstein, R. (1999) The catalytic reaction and inhibition mechanism of Drosophila alcohol dehydrogenase: observation of an enzyme-bound NAD-ketone adduct at 1.4 A resolution by X-ray crystallography. *J. Mol. Biol. 289*, 335−355.

(21) Stivala, A., Wybrow, M., Wirth, A., Whisstock, J. C., and Stuckey, P. J. (2011) Automatic generation of protein structure cartoons with Pro-origami. *Bioinformatics 27*, 3315−3316.

(22) Rossmann, M. G., Moras, D., and Olsen, K. W. (1974) Chemical and biological evolution of nucleotide-binding protein. *Nature 250*, 194−199.

(23) Meng, Q., Peng, Z., and Yang, J. (2018) CoABind: a novel algorithm for Coenzyme A (CoA)- and CoA derivatives-binding residues prediction. *Bioinformatics 34*, 2598−2604.
(24) Capyk, J. K., Kalscheuer, R., Stewart, G. R., Liu, J., Kwon, H., Zhao, R., Okamoto, S., Jacobs, W. R., Jr., Eltis, L. D., and Mohn, W. W. (2009) Mycobacterial cytochrome P450 125 (cyp125) catalyzes the terminal hydroxylation of C27 steroids. *J. Biol. Chem. 284*, 35534−35542.
(25) Driscoll, M. D., McLean, K. J., Levy, C., Mast, N., Pikuleva, I. A., Lafite, P., Rigby, S. E., Leys, D., and Munro, A. W. (2010) Structural and biochemical characterization of *Mycobacterium tuberculosis* CYP142: evidence for multiple cholesterol 27-hydroxylase activities in a human pathogen. *J. Biol. Chem. 285*, 38270−38282.
(26) Yang, M., Lu, R., Guja, K. E., Wipperman, M. F., St Clair, J. R., Bonds, A. C., Garcia-Diaz, M., and Sampson, N. S. (2015) Unraveling cholesterol catabolism in *Mycobacterium tuberculosis*: ChsE4-ChsE5 alpha2beta2 acyl-CoA dehydrogenase initiates beta-Oxidation of 3-Oxo-cholest-4-en-26-oyl CoA. *ACS Infect. Dis. 1*, 110−125.
(27) Lu, R., Schmitz, W., and Sampson, N. S. (2015) Alpha-methyl acyl CoA racemase provides *Mycobacterium tuberculosis* catabolic access to cholesterol esters. *Biochemistry 54*, 5669−5672.
(28) Schaefer, C. M., Lu, R., Nesbitt, N. M., Schiebel, J., Sampson, N. S., and Kisker, C. (2015) FadA5 a thiolase from *Mycobacterium tuberculosis*: a steroid-binding pocket reveals the potential for drug development against tuberculosis. *Structure 23*, 21−33.
(29) Xu, L. Q., Liu, Y. J., Yao, K., Liu, H. H., Tao, X. Y., Wang, F. Q., and Wei, D. Z. (2016) Unraveling and engineering the production of 23,24-bisnorcholenic steroids in sterol metabolism. *Sci. Rep. 6*, 21928.
(30) Yuan, T., Yang, M., Gehring, K., and Sampson, N. S. (2019) *Mycobacterium tuberculosis* exploits a heterohexameric enoyl-CoA hydratase retro-aldolase complex for cholesterol catabolism. *Biochemistry 58*, 4224−4235.
(31) Gilbert, S., Hood, L., and Seah, S. Y. K. (2018) Characterization of an aldolase involved in cholesterol side chain degradation in *Mycobacterium tuberculosis*. *J. Bacteriol. 200*, e00512-17.
(32) Holert, J., Jagmann, N., and Philipp, B. (2013) The essential function of genes for a hydratase and an aldehyde dehydrogenase for growth of *Pseudomonas sp.* strain Chol1 with the steroid compound cholate indicates an aldolytic reaction step for deacetylation of the side chain. *J. Bacteriol. 195*, 3371−3380.
(33) Warnke, M., Jacoby, C., Jung, T., Agne, M., Mergelsberg, M., Starke, R., Jehmlich, N., von Bergen, M., Richnow, H. H., Bruls, T., and Boll, M. (2017) A patchwork pathway for oxygenase-independent degradation of side chain containing steroids. *Environ. Microbiol. 19*, 4684−4699.
(34) Warnke, M., Jung, T., Jacoby, C., Agne, M., Feller, F. M., Philipp, B., Seiche, W., Breit, B., and Boll, M. (2018) Functional characterization of three specific acyl-coenzyme A synthetases involved in anaerobic cholesterol degradation in *Sterolibacterium denitrificans* Chol1S. *Appl. Environ. Microbiol. 84*, e02721-17.
(35) Casabon, I., Swain, K., Crowe, A. M., Eltis, L. D., and Mohn, W. W. (2014) Actinobacterial acyl coenzyme A synthetases involved in steroid side-chain catabolism. *J. Bacteriol. 196*, 579−587.
(36) Griffin, J. E., Gawronski, J. D., Dejesus, M. A., Ioerger, T. R., Akerley, B. J., and Sassetti, C. M. (2011) High-resolution phenotypic profiling defines genes essential for mycobacterial growth and cholesterol catabolism. *PLoS Pathog. 7*, No. e1002251.
(37) Sassetti, C. M., and Rubin, E. J. (2003) Genetic requirements for mycobacterial survival during infection. *Proc. Natl. Acad. Sci. U. S. A. 100*, 12989−12994.
(38) Van der Geize, R., Yam, K., Heuser, T., Wilbrink, M. H., Hara, H., Anderton, M. C., Sim, E., Dijkhuizen, L., Davies, J. E., Mohn, W. W., and Eltis, L. D. (2007) A gene cluster encoding cholesterol catabolism in a soil actinomycete provides insight into *Mycobacterium tuberculosis* survival in macrophages. *Proc. Natl. Acad. Sci. U. S. A. 104*, 1947−1952.
(39) Ishibashi, T., and Bloch, K. (1981) Intermembrane transfer of 5 alpha-cholest-7-en-3 beta-ol. Facilitation by supernatant protein (SCP). *J. Biol. Chem. 256*, 12962−12967.
(40) Seedorf, U., Brysch, P., Engel, T., Schrage, K., and Assmann, G. (1994) Sterol carrier protein X is peroxisomal 3-oxoacyl coenzyme A thiolase with intrinsic sterol carrier and lipid transfer activity. *J. Biol. Chem. 269*, 21277−21283.
(41) Holert, J., Brown, K., Hashimi, A., Eltis, L. D., and Mohn, W. W. (2020) Steryl ester formation and accumulation in steroid-degrading bacteria. *Appl. Environ. Microbiol. 86*, e02353-19.
(42) Thomas, S. T., and Sampson, N. S. (2013) *Mycobacterium tuberculosis* utilizes a unique heterotetrameric structure for dehydrogenation of the cholesterol side chain. *Biochemistry 52*, 2895−2904.
(43) Wipperman, M. F., Yang, M., Thomas, S. T., and Sampson, N. S. (2013) Shrinking the FadE proteome of *Mycobacterium tuberculosis*: insights into cholesterol metabolism through identification of an alpha2beta2 heterotetrameric acyl coenzyme A dehydrogenase family. *J. Bacteriol. 195*, 4331−4341.
(44) Yang, M., Guja, K. E., Thomas, S. T., Garcia-Diaz, M., and Sampson, N. S. (2014) A distinct MaoC-like enoyl-CoA hydratase architecture mediates cholesterol catabolism in *Mycobacterium tuberculosis*. *ACS Chem. Biol. 9*, 2632−2645.
(45) Gadbery, J. E., Round, J. W., Yuan, T., Wipperman, M. F., Story, K. T., Crowe, A. M., Casabon, I., Liu, J., Yang, X., Eltis, L. D., and Sampson, N. S. (2020) IpdE1-IpdE2 is a heterotetrameric acyl coenzyme A dehydrogenase that is widely distributed in steroid-degrading bacteria. *Biochemistry 59*, 1113−1123.
(46) Kabsch, W. (2010) XDS. *Acta Crystallogr., Sect. D: Biol. Crystallogr. 66*, 125−132.
(47) Evans, P. R., and Murshudov, G. N. (2013) How good are my data and what is the resolution? *Acta Crystallogr., Sect. D: Biol. Crystallogr. 69*, 1204−1214.
(48) Vonrhein, C., Flensburg, C., Keller, P., Sharff, A., Smart, O., Paciorek, W., Womack, T., and Bricogne, G. (2011) Data processing and analysis with the autoPROC toolbox. *Acta Crystallogr., Sect. D: Biol. Crystallogr. 67*, 293−302.
(49) Tickle, I. J., Flensburg, C., Keller, P., Paciorek, W., Sharff, A., Smart, O., Vonrhein, C., and Bricogne, G. (2018) *STARANISO*, Global Phasing Ltd, Cambridge, United Kingdom.

https://doi.org/10.1021/acsinfecdis.1c00069
ACS Infect. Dis. 2021, 7, 1739−1751